ACS APPLIED MATERIALS & INTERFACES

www.acsami.org

Research Article

Electric and Photovoltaic Switching by Ionic Migration with a Magnetic Record

Matthew Rogers, Ahasan Habib, Emiliano Poli, Caitlin Probert, Gilberto Teobaldi, Nader Alosaimi, Timothy Moorsom, Zabeada Aslam, Gavin Burnell, Mannan Ali, Bryan J. Hickey, and Oscar Cespedes*

Cite This: *ACS Appl. Mater. Interfaces* 2026, 18, 41881−41888

Read Online

ACCESS | Metrics & More | Article Recommendations | Supporting Information

ABSTRACT: Combining optical and magnetic functionalities into memristors is an attractive option to expand applications into image recognition, information storage, and low power processing. Here, we have fabricated ferromagnetic-fullerene-manganese oxide structures that display a hysteretic, nonlinear *I*–*V* characteristic and a photovoltaic effect with a photocurrent dependent on the relative alignment of the magnetization and the light polarization vector. Reversible, voltage-induced oxygen migration from manganese oxide into the molecular layer reduces the resistivity of the device by several orders of magnitude, eliminates the nonlinear transport, and quenches the photovoltaic response, giving rise to an optically sensitive memristor where the photocurrent is dependent on both the electrical and magnetic history of the device. Density functional theory calculations attribute the origin of these effects to changes in the electronic structure at the Fermi level and a reduction of the interface dipole upon ionic migration. These results open research pathways towards single-molecule scale memristive memories with optical excitation, electrical readout and magnetic sensing functionalities.

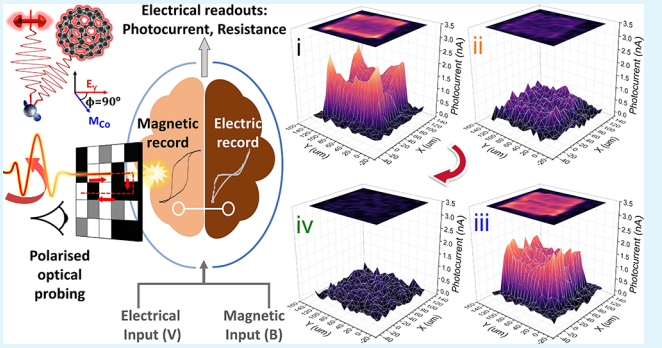

KEYWORDS: *memristor, molecular spintronics, metal-oxide, fullerene, light polarization, photocurrent*

1. INTRODUCTION

Ionic displacement is a common mechanism to the operation of memristors, with applications in sensors, memories and artificial synapses for neuromorphic computing.[1−3] Ionic dynamics have also been discussed as a possible means to control electrically magnetic properties of hybrid magneto-oxide structures, leading to applications in information storage.[4−9] Magneto-ionic[10,11] and opto-ionic[12,13] memristors have also been considered for artificial neural networks with low power of operation and reduced learning steps.[14] This has led to the field of bioinspired ionotronic neural computing. Ionic migration in molecular spintronics has been explored to control the response of organic spin valves, with both fluorine atomic diffusion[15] and oxygen impurities changing the magnetoresistance of the device.[16] In order to mimic the flexibility of neural operation, with visual recognition, hysteresis, and the replication of biological responses to a variety of stimuli with an electrical readout, it is key to develop structures with extended functionalities where the input/output is dependent not just on one of electrical, magnetic or optical signals but also on a combination thereof and the history of the device. For example, optical inputs can be used for self-powering readout of photoactive oxide hybrid memristors,[17] oxide-based hybrid random access memories,[18] and optoelectronic memristors for neuromorphic computing.[19] Adding functionalities leads to architectures that can imitate different bioprocesses, combining electro-magnetic read/write with optical sensitivity.

Here, we present results in metal-molecular-metal oxide multilayers, where large resistance changes are observed under both optical irradiation and electric bias. Furthermore, when using a magnetic electrode, a photocurrent is measured and dependent on the relative alignment of the magnetization of the electrode with respect to the light polarization. The structure has, therefore, two independent memory capabilities; magnetic and electrical, both of which can be probed optically and independently of each other. The combination of three different functionalities, electrical, magnetic, and optical, make of these structures an interesting platform for complex operations, or when different responses are needed to an array of environmental signals. The structure is scalable and could potentially be reduced to

Received: February 10, 2026
Revised: July 7, 2026
Accepted: July 9, 2026
Published: July 21, 2026

https://doi.org/10.1021/acsami.6c02910
ACS Appl. Mater. Interfaces 2026, 18, 41881−41888

nanoscale or single molecule devices. Although the switching process can be detected electrically in the form of a change in the molecule's conductance, adding spin and optical functionalities to molecular memories is particularly relevant, for example, in the recording of high resolution visual information and image recognition via transmission of optical irradiation through patterns, with the wavelength and light intensity transmitted altering the device photovoltaic response, see schematic in Figure 1a.[20]

2. EXPERIMENTAL SECTION

Cobalt, platinum, manganese, and fullerene thin films were grown without breaking vacuum at a base pressure of ≈10^{-8} mTorr. Metals were deposited via DC magnetron sputtering (Pt, Co, Mn, and Al), followed by plasma oxidation to form MnO_x on a glass transparent insulating substrate. Oxygen content varies across the film and depending on the electrical bias applied, with MnO_2 the most stable form in ambient conditions. The Co layer acts as metal electrodes and also as ferromagnetic element for the magnetic record response of the device. Pt/Co multilayers are used as electrode with perpendicular magnetic anisotropy (PMA) when tuning the stray magnetic fields and magnetic domain structure. C_{60} layers are thermally evaporated at ≈450 °C. The molecules are optically active, absorbing a wide range of wavelengths in the visible range with photoluminescence at 1.69 eV. The fullerenes are also highly resistant to metal growth, forming polycrystalline films with a typical grain size of several tens of nm. A 2 nm thick Al film is deposited over the device and passivates upon exposure to atmosphere, forming a protective Al_2O_3 layer that prevents degradation. The four-point resistance of the $Co/C_{60}/MnO_x$ devices is of the order of MΩ for a typical 100 × 100 μm^2 junction area (junctions with 200 × 100 μm^2 surface were also measured, these are identified in the captions). The metal oxide electrode acts as an ionic reservoir, providing the oxygen migrating into the fullerene layer to switch resistivity and photovoltaic states. However, the MnO_x electrode can have a very high resistance that reduces the photocurrent. The MnO_x is the *p*-electrode and connected to the positive bias terminal. Photovoltaic measurements are carried out in a microscope using a 50x objective, a mapping mechanical stage with sub-μm step control and three lasers at 633, 532, and 473 nm. Shorter wavelengths generate a higher photocurrent, but may lead to device degradation via polymerization of the fullerenes at powers above some 1 kW/cm^2. It is possible to reverse the switching of the device for over 30 cycles, but exceeding voltage thresholds of 8–12 V leads to an irreversible low-resistance state, probably due to the formation of filaments as observed in, e.g., photovoltaic ferroelectrics.[21] The characteristic switching time of the device is of the order of seconds at room temperature in a 100 × 100 μm^2 junction 20 nm thick (Supporting Information Figure S1). For an oxygen concentration of approximately 0.1 atoms per molecule in the low resistance state, the change in concentration for oxygen atoms, Δc, would be 1.4×10^{26} m^{-3}. With a diffusion time of the order of one second, the flow density of oxygen particles over the C_{60} junction, J_{flow}, is then ~2.8×10^{18} m^{-2}s^{-1}. The diffusion coefficient (J_{flow} over Δc and the junction thickness) is then $D \sim 10^{-12}$ cm^{2}s^{-1}, similar to values found in thin film solid state Li-based battery electrolytes and cathodes.[22,23]

Collinear, van der Waals (vdW) corrected DFT simulations were performed using the projected augmented wave (PAW) formalism as implemented in the VASP program.[24−26] We used the PBE exchange-correlation (XC) functional,[27] a 400 eV plane wave energy cut-off, and, unless otherwise stated, a 2 × 2 × 1 Monkhorst–Pack *k*-point grid.[28] A Gaussian smearing of 0.1 eV width was used in all the calculations. We applied anisotropic Hubbard corrections [DFT+(U–J)][29] to the 3d orbitals of the Mn atoms (U = 6.1 eV and J = 1.0 eV) to ameliorate the limitations of the PBE-XC functional in describing manganese oxides. VdW corrections were applied using the Grimme parameterization.[30] Geometry optimizations, with inclusion of dipole corrections, were performed by fully relaxing all atoms in the systems within a tolerance of 0.02 eV/A on the atomic forces. A vacuum buffer of 15 Å along the nonperiodic direction was added to all systems considered. Bader charge analysis[31] was carried out based on the total charge density, accounting for both the electronic and ionic core charges. Electrostatic interface dipoles perpendicular to the interface

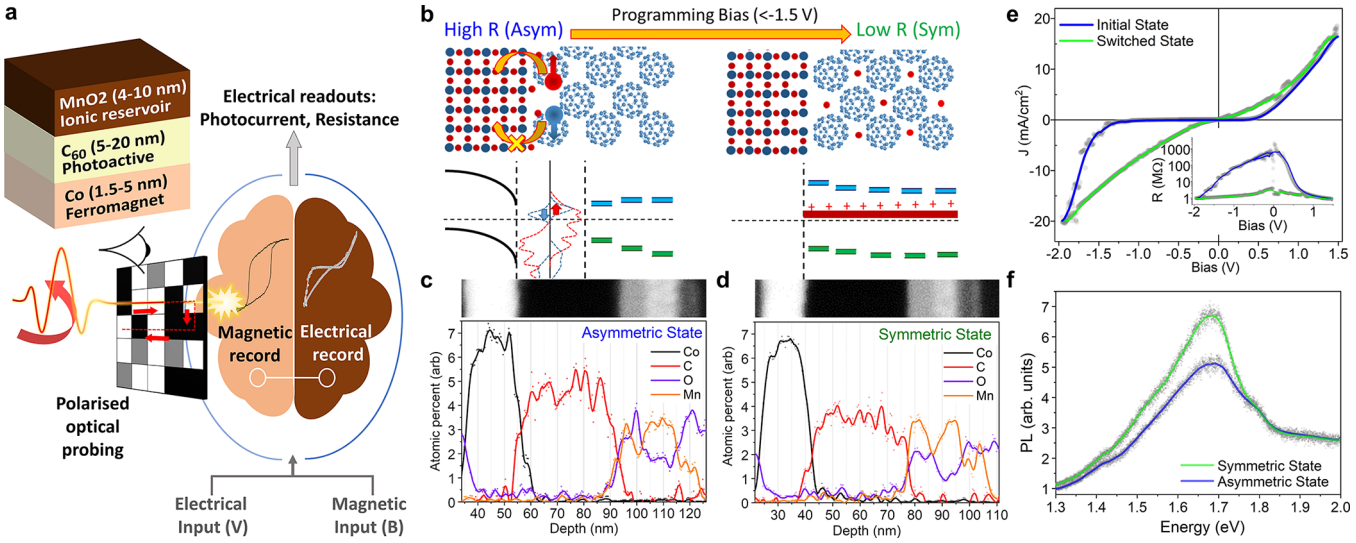

Figure 1. Memristive effect in $Co/C_{60}/MnO_x$ due to oxygen migration into the molecular layer. (**a**) Schematic of the functionalities of each layer, with electrical and magnetic memory operations and polarization-dependent optical probing. (**b**) Oxygen ion migration under an applied voltage. Transmission electron cross section images elemental analysis in the (**c**) asymmetric state before switching, and (**d**) in the more symmetric state with lower resistance after the oxygen is pushed into the molecular layer for a $Co(25)/C_{60}(40)/MnO_x(30)$ thicknesses in brackets in nm. (**e**) Typical current–voltage characteristic of a device with hysteresis effects appearing for voltages above 1–1.5 V in a $Co(5)/C_{60}(20)/MnO_x(10)$ device. Before switching, the *I*–*V*is highly asymmetric, with a factor 20 difference in the resistance for positive (R≈ 200 MΩ) and negative (R ≈ 12.5 MΩ) 0.5 V bias, but becomes symmetric after switching to the low resistance state (R≈ 1.8 MΩ at + and –0.5 V). (**f**) Change in the C_{60} photoluminescence (PL) under irradiation with red light (633 nm) after oxygen migration in this device, which breaks the dipolar field and decreases the exciton lifetime. Lines are a guide to the eye from the smoothed data. Error bars not shown are too small to display.

https://doi.org/10.1021/acsami.6c02910
ACS Appl. Mater. Interfaces 2026, 18, 41881−41888

plane were calculated using the standard procedure implemented in VASP for dipole corrected calculations.

3. RESULTS AND DISCUSSION

In their pristine state, the *I*–V characteristic of Co/C_{60}/MnO_x devices is nonlinear and asymmetric, with rectification factors, the resistance ratio measured at 0.5 V positive and negative voltages, of up to 20–30. The resistance of the device drops by up to three orders of magnitude after a large negative electric bias, and the *I*–*V*becomes more symmetric, with a lower rectification factor. The resistance switching is about one order of magnitude smaller than for state-of-the-art hybrid P3HT:PCBM optical memristors.[17] The resistance change and rectification are reversible with an applied voltage of reverse polarity. We attribute the changes to the displacement of oxygen atoms from the MnO_x–C_{60} interface into the molecular layer, an effect confirmed by elemental mapping in transmission electron microscopy of cross-section images of the multilayer (Figure 1c,d). The *I*–V characteristic is similar to that of Monazomycin-formed ion channels in lipid membranes that mimic neuronal behavior, albeit with one order of magnitude higher voltage threshold.[32]

The structure has a photovoltaic response under laser irradiation due to exciton generation at the molecular layer and splitting via the dipolar electric fields at the interfaces,[33,34] with open circuit voltages (V_{OC}) of the order of 0.3 V and short circuit photocurrent densities (J_{SC}) of 10 mA/cm^2 for excitation powers of the order of 100 W/cm^2. We find that the photovoltaic effect is only present when C_{60} is interfaced with some transition metals such as Cu and Co, and is absent when interfaced with, e.g., Ta, Al, or Au, see Supporting Information Figure S2. This is probably due to a good alignment of the Fermi level of the former metals with the LUMO of the molecules. C_{60} metalizes on Cu and Co due to strong binding and large interface dipole density, with charge going from the metal to fullerene. This leads to strong electrical dipoles at the metallo-molecular interface that breaks the excitons and forms the photocurrent. At the other side of the junction, MnO_x acts as an electron sink and the electrostatic field is acting in the same direction. The photocurrent has a strong inverse dependence with the thickness of the metal electrode that can be explained as due to changes in the metal work-function and nonradiative energy transfer, with the electric dipole of the molecular exciton transferring the energy to the metal surface plasmons in thinner films and not contributing to the electrical current (Figure S2).[35,36] Because our devices are fabricated by shadow masking, the thickness of the layers is not uniform, with slightly thinner C_{60} and electrodes near the edges. This leads to a larger photocurrent at the edges of the junction.

Oxygen causes a 4-fold decrease of the exciton lifetime and typically a 20% reduction in the open-circuit voltage of fullerene-based solar cells.[37] After moving oxygen into the C_{60} layer, in our devices there is an increased photoluminescence and a drop in the short circuit photocurrent, see Figures 1f and 2a–c. Both the resistance and photocurrent recover after applying a bias in the opposite direction to move the oxygen back across the interface into the oxygen-depleted MnO_x film. Given that the electronegativity of oxygen is 3.44 eV and that of manganese 1.55 eV, it is energetically unfavorable for electrons to remain bound to manganese when oxygen is displaced. Furthermore, the increased photoluminescence is indicative of the presence of additional charges at the molecular layer in the low resistance state, so the oxygen is mostly likely to be displaced as an ion. This can also be seen in the DFT models of the structure before and after switching (See Figures S8 and S9 in the Supporting Information). The memristive effect is, therefore, linked to the capability of switching on/off the photovoltaic output in fullerene/metal oxide bilayer via reversible voltage-induced oxygen diffusion and changes to the interfacial dipole.[33,34] Raman measurements of the junction in the high and low resistance state before and after several switching cycles show no evidence of oxidation or polymerization of the C_{60} cages, with a sharp Ag(2) mode peak at 1469 cm^{-1} that is slightly narrower in the low-resistance switched state but does not shift in frequency, so the oxygen is likely to remain interstitial (Supporting InformationFigure S3).[38,39] A Raman map after switching does not show changes in the Ag(2) mode peak width over the junction, so changes are not localized to certain regions of the junction, at least within the ∼2 μm resolution of the microscope over which the signal is averaged. Changes in the peak width could be due to breaking of the hybridization with manganese oxide at the interface (Supporting Information Figure S3).[40]

The photovoltaic response of the device is highly sensitive to the electric bias history. Applying increasingly large negative voltages results in lower photocurrent and open circuit voltage that can be recovered with positive voltages up to 6–7 V, see Figure 2d. For applied bias above 8 V, the device is irreversibly changed into a low resistance state as mentioned above. After switching with an applied negative voltage, the device can also switch back to the original high resistance state without a positive bias if left under optical irradiation for several minutes to hours. Light exposure accelerates the return to a high-resistance state due to photoassisted oxygen migration, with factor 10 higher diffusivity under light exposure.[41] The switching time is inversely dependent on the resistance value after applying a negative bias, i.e. a lower resistance is reached and a longer reversal time under light exposure is observed when more oxygen has been displaced, see Figure 2e. The photoconductance of the device is also related to the presence of oxygen in the C_{60} layer, with a linear dependence between the photoconductance and the device resistance (Figure 2f). The effect of light irradiation on the differential resistance (photoresistance) of the device is shown in Figure 2g.

To investigate the effects of oxygen migration on the electronic and photovoltaic properties of the C_{60}/MnO_2 interface, we carried out collinear, van der Waals-corrected density functional theory (DFT) calculations. Starting from the energy-favored, oxidized and chemically bound (o-chem) C_{60}/MnO_2(110)–2x2 geometry (Figure 3a–c),[33] we optimized 72 different structures by displacing each individual oxygen along the z-axis on the MnO_2(110) surface at three different distances: near the oxide surface, between the two C_{60} molecular layers and on top of two C_{60} molecules; see Figure 3d,e and Supporting Information. Adopting this combinatorial strategy, we explored a grid of possible sites where the oxygen atom could diffuse during the migration dynamics. When unphysical overlaps between C_{60} and the displaced oxygen atoms presented in the automatic setup of the systems, we repositioned the oxygen atom, moving it along the *z*-axis if possible or within the *xy*-plane otherwise to the nearest location where its distance from the carbon atoms was at least 2.0 Å.

O-diffusion from the MnO_2 ionic reservoir film into the C_{60} can populate different metastable states with overall strong suppression of the interfacial dipole and associated electrostatic

https://doi.org/10.1021/acsami.6c02910
ACS Appl. Mater. Interfaces 2026, 18, 41881−41888

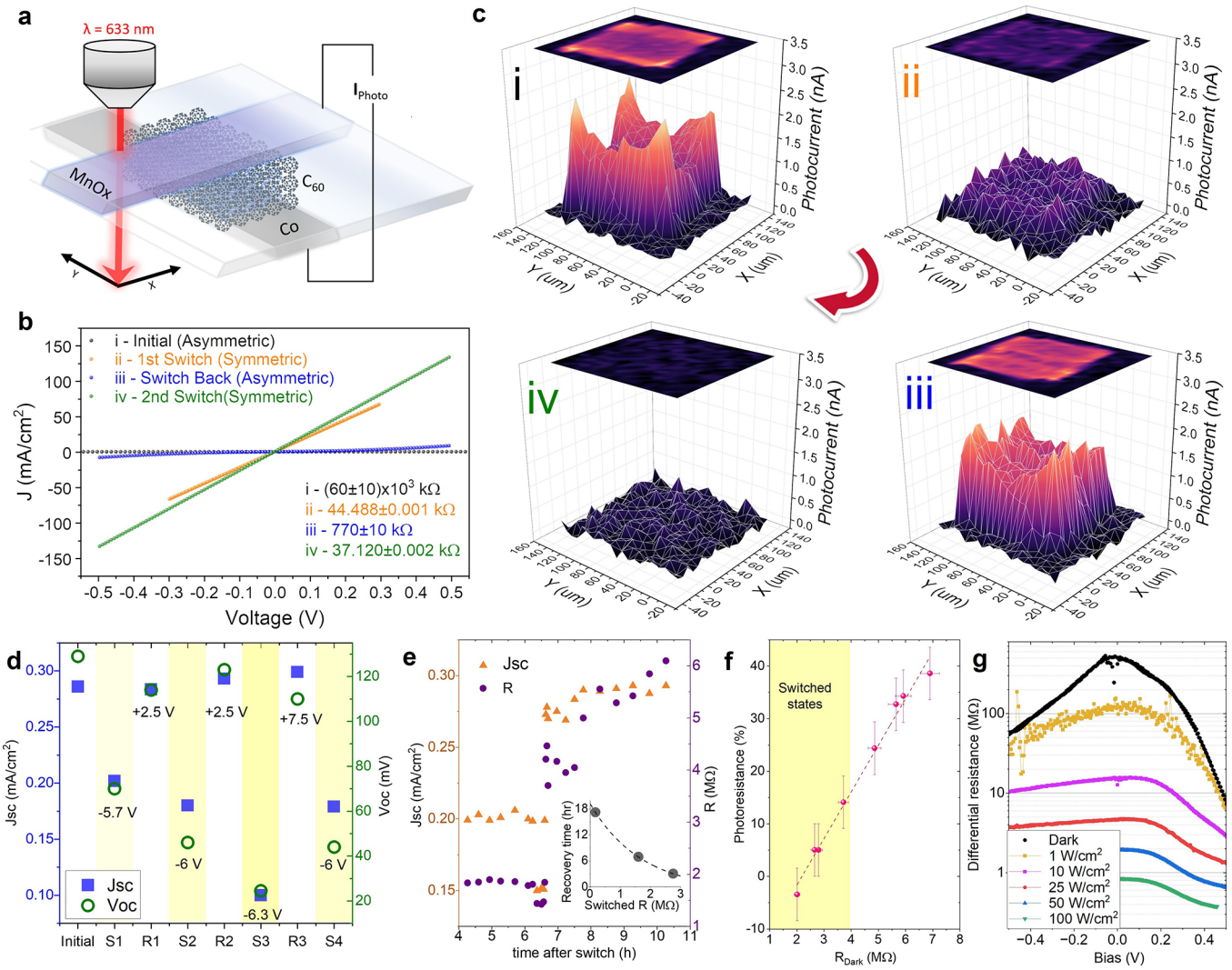

Figure 2. Photovoltaic switching due to ionic displacement in a Co(5)/C_{60}(20)/MnO_x(10) structure-thicknesses in brackets in nm. (**a**) Schematic of the measurement setup where a laser focused by an optical microscope is used for photovoltaic probing. The sample is placed on a mechanical stage that allows for the mapping of the response. (**b**) *I*–*V* characteristic of the device in the four probed states; two with high resistance and *I*–*V* asymmetry, and two low resistance with symmetric transport after an applied –2.5 V bias. (**c**) Corresponding photocurrent maps across the junction device. Higher photocurrent near the edge of the structure is due to a thinning of the layers caused by sputtering through a metal shadow mask. (**d**) Photovoltaic response for different resistance states. Low resistance switching after an applied negative voltage shaded in yellow. Original state recovered with a positive voltage. (**e**) Short-circuit photocurrent and device resistance after a negative voltage. The original high resistance state emerges again after several hours under continuous exposure to red light. The sudden change in current and resistance is associated to the re-formation of the interfacial dipole as oxygen migrates close to the MnO_x surface. Inset: The time needed for the recovery is inversely proportional to the resistance value in the switched state. (**f**) Photoresistance vs resistance in the low resistance switched state (yellow shade) and high resistance state. (**g**) Bias-dependent resistivity as a function of the light intensity. All measurements under 100 W/cm^2, 633 nm light irradiation.

field, therefore, quenching the photovoltaic effect (see Supporting Information Table S1 and Figure 3f–h). As the pristine interface presents electronic transfer from the C_{60} molecules contacted to the MnO_2 substrate (Supporting Information and ref 34), to a first approximation this change can be understood as originating from the motion of negatively charged O-atoms from an initially negative MnO_2 substrate into a positively charged C_{60} film, with ensuing reduction of the charge separation across the MnO_2/C_{60} contact and the ensuing interface dipole sustaining the photocurrent. The simulations of the modified C_{60}/MnO_x systems reveal that O-atom (ion) diffusion into the C_{60} film introduces minority-spin empty gap states not present in the pristine half-metallic C_{60}/MnO_x interface.[26,27] In parallel, the LUMO of the C_{60} molecules contacted to the diffusing O-atoms undergoes a ~0.8 eV downward shift toward the Fermi level (Figure S9 and Supporting Information). Together, these effects open additional electronic transport pathways, which is consistent with the experimentally observed decrease in resistance.

Both J_{SC} and V_{OC} can be monitored as a function of the light polarization and magnetic history of the device, see Figure 4a. Photomagnetic modulation has been put forward as a mechanism for multidimensional spin-optolelectronic strained magnetic devices.[42] The optical signal is dependent not only on the resistance state of the device but also on the spin order of

https://doi.org/10.1021/acsami.6c02910
ACS Appl. Mater. Interfaces 2026, 18, 41881–41888

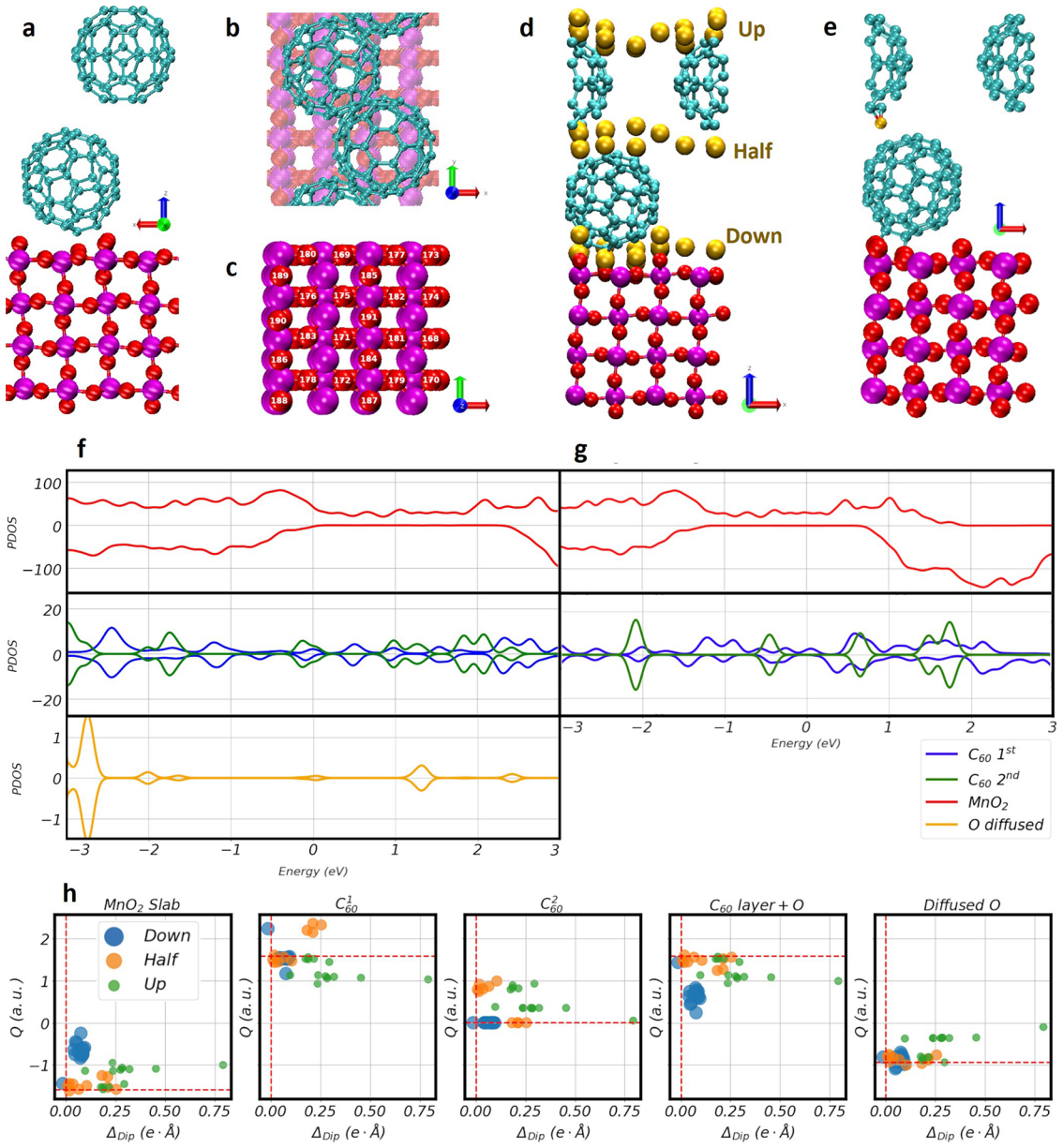

Figure 3. Side (**a**) and top (**b**) view of the optimized, starting $C_{60}/C_{60}/MnO_2(110)$–2x2 geometry. (**c**) Top view of the system without showing the C_{60} molecules, with oxygen atom indices reported in white. Color code: C-cyan, Mn-purple, and O-red. (**d**) Cumulative visualization of the initial geometries for the 72 structures created by systematically displacing each O atoms at the MnO_2 surface: near the surface ("down" structures), between the two C_{60} molecules ("half" structures), and on top of the two C_{60} molecules ("up" structures). (**e**) Optimized geometry for the oxygen ion #189 displaced to the half position. Atom-resolved projected density of states (PDOS) for the optimized systems with the #189 oxygen ion in the half position, (**f**) and in the pristine state, (**g**) calculated Fermi level is set as 0 eV reference. Note the shift in the MnO_x electronic structure and changes in the available states at the Fermi level of the two molecular layers after ion displacement. (**h**) Plot of the net charges for the different components and species of the 38 $C_{60}/MnO_2(110)$ interface models as a function of the change in interface dipole, with positive changes reducing its absolute value, and color-coded to differentiate between the down, half and up geometries for the diffusing O-atoms. The horizontal and vertical red lines mark the results for the initial pristine structure. Further detail and models can be found in the Supplementary Information.

the magnetic electrode. We find a change of 20–40% in J_{SC} and 10–20% in V_{OC} as a function of the angle, ϕ, between the magnetization of the cobalt electrode with the polarization of the incident light. Light polarization effects can take place in hybrid spintronic photovoltaic devices due to chirality-dependent excitation of spin up/down electrons with clockwise/counterclockwise circularly polarized light.[43,44] However, in our measurements the measurements are dependent on the alignment of linearly polarized light; therefore, the same number of spin up and down electrons should be generated. The result is, therefore, unlikely to be due to spin dependent hopping/tunneling at the molecular or oxide layers. We attribute this difference in photocurrent with linearly polarized light to changes in reflectivity due to the quadratic Kerr effect, Figure 4b. Lower (higher) J_{SC} is observed when the magnetic electrode has previously been aligned parallel (perpendicular) to the light polarization, see Figure 4c–e and Supporting Information Figure S5. This light polarization vs magnetization effect depends on the electrical record of the device, i.e., whether

https://doi.org/10.1021/acsami.6c02910
ACS Appl. Mater. Interfaces 2026, 18, 41881−41888

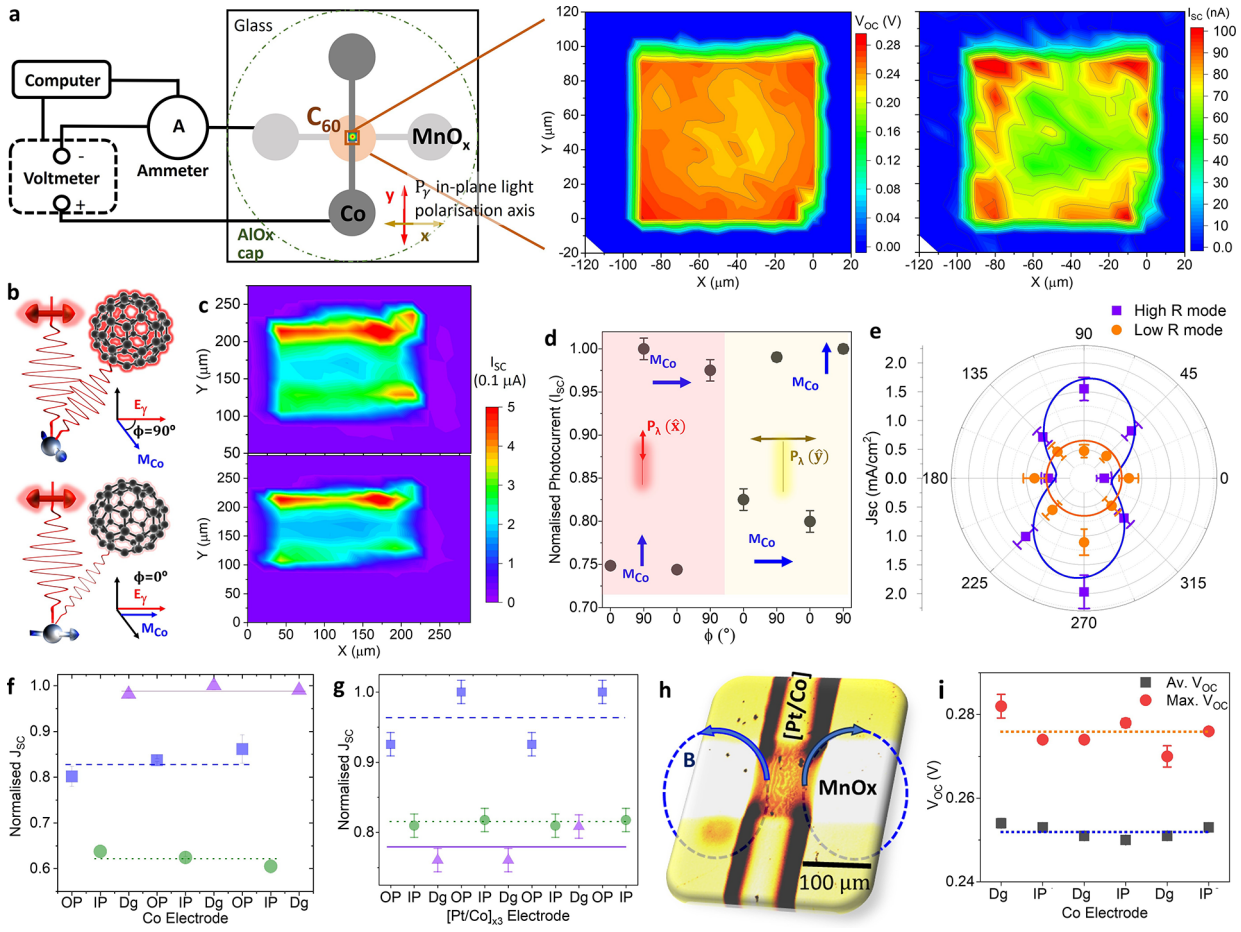

Figure 4. (**a**) Schematic of the photovoltaic measurements setup with the light polarization axis and examples of short circuit photocurrent, J_{SC}, and open circuit voltage, V_{OC}, maps of the response in the junction active area. Note the comparative uniformity of V_{OC} relative to J_{SC} across the junction due to the strong dependence of the photocurrent on the electrode's thicknesses, which is reduced on the edges of the Co(10)/C_{60}(20)/MnO_x(10) device. Blue light (473 nm) with 1 mW power (partly refracted by the top electrode over the junction area), was used for photovoltaic excitation in all the results that follow. (**b**) Schematic on the effect on the angle ϕ between light polarization (E_γ) and magnetization (M_{Co}). When the magnetization is parallel to the light polarization, there is a reduction in the photocurrent measured. (**c**) Maps of the photocurrent in a Co(5)/C_{60}(15)/MnO_x(10) 200 × 100 μm junction when the light polarization is (top) perpendicular (ϕ = 90°), and (bottom) parallel (ϕ = 0°) to the Co electrode magnetization. (**d**) The total photocurrent in a device is increased at ϕ = 90° for either vertically or horizontally polarized light. (**e**) Dependence of J_{SC} on ϕ for a pristine device and after a switch to a lower resistance state. Normalized J_{SC} as a function of the magnetic history of the device (OP – after saturation in an out-of-plane field; IP – after an in-plane field; Dg – after degaussing) for a (**f**) Co/C_{60}/MnO_x device with in-plane easy axis, and (**g**) a $[Pt(1.5)/Co(0.5)]_{x3}$ electrode with PMA. (**h**) Magneto-optic Kerr microscope images of the [Co/Pt] electrode after degaussing show the remanent maze domain magnetic structure at the junction. (**i**) V_{OC} measurements do not show sensitivity to the magnetic history of the device. All measurements in (**d–g,i**) correspond to photocurrent averages of maps over the junction area. Thicknesses in brackets in nm.

a negative (low short-circuit photocurrent, J_{SC}) or positive voltage (high J_{SC}) has been applied. After a factor 10 reduction in the resistance of device induced with a negative bias, the dependence of the photovoltaic effect on light polarization appears to be quenched, Figure 4e. This could be due to the measurement of an effect over a much smaller signal (lower photovoltaic current after switching to the low resistance state) or to the migrated oxygen altering the magnetic structure of the layers and interfaces. The photocurrent depends as well on the magnetic history of the device via its domain structure. Conventional Co/C_{60}/MnO_x devices with an in-plane anisotropy show higher J_{SC} after the magnetic electrode has been disordered with an out-of-plane field, and even more so after fully degaussing the electrode to zero magnetization with a decaying AC field, Figure 4f. In contrast to the single layer Co electrode, $[Pt/Co]_{\times n}$/C_{60}/MnO_x devices with a superlattice multilayer magnetic electrode that has perpendicular magnetic anisotropy (PMA) show a different behavior. These structures generate a strong stray field in the (out-of-plane, OOP) saturated state that reduces spin-dependent charge accumulation at the interface, increasing the current J_{SC} for the PMA saturated state, Figure 4g. Demagnetizing the PMA structure now generates a maze-domain state that reduces the stray field at the interface (Figure 4h), reducing the current. This is the opposite effect seen for in-plane devices, as there the stray field, and therefore J_{SC}, are maximized by degaussing the system. The open circuit voltage V_{OC} does not show a dependence on the magnetic domain structure, Figure 4i. V_{OC} can depend on the angle ϕ, but the dependence is weaker than in J_{SC}, with changes of only a few percent, see Supporting Information Figure S5. As it could be expected, Cu/C_{60}/MnO_x devices without a magnetic electrode do not show a dependence on the magnetic history of the device

https://doi.org/10.1021/acsami.6c02910
ACS Appl. Mater. Interfaces 2026, 18, 41881–41888

when averaged over several measurements (Supporting Information Figure S6).

4. CONCLUSIONS

Our results show that it is possible to displace reversibly oxygen ions from a manganese oxide reservoir into a molecular C_{60} layer. The ions alter the electronic states and exciton lifetime of the fullerenes, leading to changes in the resistivity and luminescence of the structure. By adding metal electrodes with a good alignment of the Fermi level and the LUMO molecules, we can achieve strong charge transfer that forms an interfacial dipole. The dipoles formed at both molecular interfaces split excitons and carry electrons (holes) towards the oxide (metal), leading to a photovoltaic response. This photovoltaic response is quenched upon oxygen diffusion into the molecular layer. Furthermore, by using a ferromagnetic metal, we can add functionalities where the photocurrent is dependent on the relative alignment of the magnetization with the light polarization and with the magnetic history/domain structure of the device. The net result is a functional multilayer structure where the resistance and photocurrent output is dependent on the electric and magnetic record—a magnetic field-dependent-memristor that acts as well as photovoltaic switch. Our devices are in the sub-mm scale, and reducing the junction size by using, e.g., nanopatterned pillar junctions could lead to more reliable and faster switching, ideally down to the molecule scale. However, problems with fullerene degradation due to the use of chemicals in optical and e-beam patterning need to be overcome, and going below the 10–20 nm scale may result in device-to-device variations in C_{60} growth. The results pave the way to combine magnetic and electric recording with photoexcitation in nondissipative spin transport, magnetic information storage and magnetic dynamics to electrical functionalities, for example, to recognize and store visual inputs in neuromorphic memristive networks.

■ ASSOCIATED CONTENT

Supporting Information

The Supporting Information is available free of charge at https://pubs.acs.org/doi/10.1021/acsami.6c02910.

Additional results, including transport and photovoltaic measurements, and DFT computational work supplied as Supporting Information (DOCX)

■ AUTHOR INFORMATION

Corresponding Author

Oscar Cespedes – *School of Physics & Astronomy, University of Leeds, Woodhouse Lane w/n, Leeds LS2 9JT, United Kingdom;* orcid.org/0000-0002-5249-9523; Email: o.cespedes@leeds.ac.uk

Authors

Matthew Rogers – *School of Physics & Astronomy, University of Leeds, Woodhouse Lane w/n, Leeds LS2 9JT, United Kingdom*

Ahasan Habib – *School of Physics & Astronomy, University of Leeds, Woodhouse Lane w/n, Leeds LS2 9JT, United Kingdom; Science, Engineering & Technology School, Khulna University, Khulna 9208, Bangladesh*

Emiliano Poli – *Department of Chemical Sciences, University of Padova, Via Francesco Marzolo, 1, Padova 35131, Italy*

Caitlin Probert – *School of Physics & Astronomy, University of Leeds, Woodhouse Lane w/n, Leeds LS2 9JT, United Kingdom*

Gilberto Teobaldi – *Scientific Computing Department, Science & Technology Facilities Council UKRI, Rutherford Appleton Laboratory, Didcot OX11 0QX, United Kingdom;* orcid.org/0000-0001-6068-6786

Nader Alosaimi – *School of Physics & Astronomy, University of Leeds, Woodhouse Lane w/n, Leeds LS2 9JT, United Kingdom*

Timothy Moorsom – *School of Physics & Astronomy, University of Leeds, Woodhouse Lane w/n, Leeds LS2 9JT, United Kingdom*

Zabeada Aslam – *School of Physics & Astronomy, University of Leeds, Woodhouse Lane w/n, Leeds LS2 9JT, United Kingdom*

Gavin Burnell – *School of Physics & Astronomy, University of Leeds, Woodhouse Lane w/n, Leeds LS2 9JT, United Kingdom*

Mannan Ali – *School of Physics & Astronomy, University of Leeds, Woodhouse Lane w/n, Leeds LS2 9JT, United Kingdom*

Bryan J. Hickey – *School of Physics & Astronomy, University of Leeds, Woodhouse Lane w/n, Leeds LS2 9JT, United Kingdom*

Complete contact information is available at: https://pubs.acs.org/doi/10.1021/acsami.6c02910

Notes

The authors declare no competing financial interest.

■ ACKNOWLEDGMENTS

We thank the Engineering and Physical Sciences Research Council in the UK for financial support via the grants EP/S030263/1, EP/S031081/1 and EP/X027074/1. G.T. acknowledges access to ARCHER2 through the UKCP consortium (EP/X035891/1) and to the SCARF-HPC facility at the STFC. E.P. acknowledges the Quantum Computing and Simulation Center (QCSC) at Padova university, and the ICSC National Center.

■ REFERENCES

(1) Sun, T. M.; Feng, B.; Huo, J. P.; Xiao, Y.; Wang, W. A.; Peng, J.; Li, Z. H.; Du, C. J.; Wang, W. X.; Zou, G. S.; Liu, L. Artificial Intelligence Meets Flexible Sensors: Emerging Smart Flexible Sensing Systems Driven by Machine Learning and Artificial Synapses. *Nano-Micro Lett.* **2024**, *16* (1), No. 14.

(2) Gao, S.; Liu, G.; Yang, H. L.; Hu, C.; Chen, Q. L.; Gong, G. D.; Xue, W. H.; Yi, X. H.; Shang, J.; Li, R. W. An Oxide Schottky Junction Artificial Optoelectronic Synapse. *Acs Nano* **2019**, *13* (2), 2634−2642.

(3) Zamarreño-Ramos, C.; Camuñas-Mesa, L. A.; Pérez-Carrasco, J. A.; Masquelier, T.; Serrano-Gotarredona, T.; Linares-Barranco, B. On spike-timing-dependent-plasticity, memristive devices, and building a self-learning visual cortex. *Front. Neurosci.* **2011**, *5*, No. 26.

(4) Wood, J. M.; Oseghale, C. I.; Cespedes, O.; Grell, M.; Allwood, D. A. Control of ferromagnetic properties of $Ni_{80}Fe_{20}$ thin films by voltage-induced oxidation. *J. Appl. Phys.* **2018**, *124* (8), No. 085304.

(5) Kang, J. H.; Lee, S.; Lee, T. H.; Yang, J. S.; Lee, J. W.; Tae, C. C.; Jeong, J. R.; Park, S. Y.; Park, B. G.; Kim, K. J. Control of electrical resistance and magnetoresistance by electric-field-driven oxygen ion migration in a single GdO_x wire. *NPG Asia Mater.* **2020**, *12* (1), No. 44.

(6) Tran, B. X.; Yang, S.; Kim, H. J.; Ha, J. H.; Yoon, S.; Kim, C.; Moon, K. W.; Choi, W. C.; Hwang, C.; Hong, J. I. Electrical Manipulation of Oxygen Ion Migrations for the Voltage-Controlled Adjustment of Magnetic Anisotropy and Optimized Skyrmion Generations. *Adv. Electron. Mater.* **2022**, *8* (12), No. 2200770.

(7) Fassatoui, A.; Ranno, L.; PeñaGarcia, J.; Balan, C.; Vogel, J.; Béa, H.; Pizzini, S. Kinetics of Ion Migration in the Electric Field-Driven Manipulation of Magnetic Anisotropy of Pt/Co/Oxide Multilayers. *Small* **2021**, *17* (38), No. 2102427.
(8) Benguettat-El Mokhtari, I.; Pachat, R.; Poreé, V.; Lamperti, A.; Roussigné, Y.; Syskaki, M. A.; Wrona, J.; Bernard, G.; Cataldo, A.; Resta, A.; et al. Exploring the full magneto-ionic oxidation spectrum in Pt/CoFeB/HfO_2. *Appl. Phys. Lett.* **2025**, *126* (23), No. 232402.
(9) Bhatnagar-Schöffmann, T.; Schöffmann, P.; Resta, A.; Lamperti, A.; Bernard, G.; Kovács, A.; Largeau, L.; Durnez, A.; Harouri, A.; Lafosse, X.; et al. Non-Oxidative Mechanism in Oxygen-Based Magneto-Ionics. *Adv. Mater. Interfaces* **2024**, *11* (14), No. 2300955.
(10) Das, S.; Mansell, R.; Syskaki, M. A.; Langer, J.; van Dijken, S. Magneto-ionic synapse for reservoir computing. *Phys. Rev. Appl.* **2025**, *23* (5), No. 054043.
(11) Nichterwitz, M.; Honnali, S.; Kutuzau, M.; Guo, S.; Zehner, J.; Nielsch, K.; Leistner, K. Advances in magneto-ionic materials and perspectives for their application. *APL Mater.* **2021**, *9* (3), No. 030903.
(12) Mohamed, E.; Tchorz, N.; Marlow, F. Iontronic memories based on ionic redox systems: operation protocols. *Faraday Discuss.* **2023**, *246*, 296−306.
(13) Wan, C. J.; Xiao, K.; Angelin, A.; Antonietti, M.; Chen, X. D. The Rise of Bioinspired Ionotronics. *Adv. Intell. Syst.* **2019**, *1* (7), No. 1900073.
(14) Xia, Z. P.; Sun, X.; Wang, Z. L.; Meng, J. L.; Jin, B. Y.; Wang, T. Y. Low-Power Memristor for Neuromorphic Computing: From Materials to Applications. *Nano-Micro Lett.* **2025**, *17* (1), No. 217.
(15) Nachawaty, A.; Chen, T. X.; Ibrahim, F.; Wang, Y. C.; Hao, Y. F.; Dalla Francesca, K.; Tyagi, P.; Da Costa, A.; Ferri, A.; Liu, C. C.; et al. Voltage-Driven Fluorine Motion for Novel Organic Spintronic Memristor. *Adv. Mater.* **2024**, *36* (33), No. 2401611.
(16) Riminucci, A.; Yu, Z. G.; Prezioso, M.; Cecchini, R.; Bergenti, I.; Graziosi, P.; Dediu, V. A. Controlling Magnetoresistance by Oxygen Impurities in Mq3-Based Molecular Spin Valves. *ACS Appl. Mater. Interfaces* **2019**, *11* (8), 8319−8326.
(17) Cai, S. Y.; Tzou, C. Y.; Liou, Y. R.; Chen, D. R.; Jiang, C. Y.; Ma, J. M.; Chang, C. Y.; Tseng, C. Y.; Liao, Y. M.; Hsieh, Y. P.; et al. Hybrid Optical/Electric Memristor for Light-Based Logic and Communication. *ACS Appl. Mater. Interfaces* **2019**, *11* (4), 4649−4653.
(18) Kumar, A.; Bhardwaj, K.; Singh, S. P.; Lee, Y.; Lee, S.; Kumar, M.; Sharma, S. K. Recent advancements in metal oxide-based hybrid nanocomposite resistive random-access memories for artificial intelligence. *InfoMat* **2025**, *7* (3), No. e12644.
(19) Wang, W. X.; Wang, Y. Q.; Yin, F. F.; Niu, H. S.; Shin, Y. K.; Li, Y.; Kim, E. S.; Kim, N. Y. Tailoring Classical Conditioning Behavior in TiO_2 Nanowires: ZnO QDs-Based Optoelectronic Memristors for Neuromorphic Hardware. *Nano-Micro Lett.* **2024**, *16* (1), No. 133.
(20) Cao, F.; Hu, Z. J.; Yan, T. T.; Hong, E.; Deng, X. L.; Wu, L. M.; Fang, X. S. A Dual-Functional Perovskite-Based Photodetector and Memristor for Visual Memory. *Adv. Mater.* **2023**, *35* (44), No. 2304550.
(21) Huang, Y. J.; Quan, Q. L.; Cheng, M. L.; Ji, J. Y.; Mo, Y. T.; Liu, Y. B.; Yu, S. J.; Lu, C. X.; Hu, L. Unveiling Ionic Conductive Filaments Enhanced Photovoltaic Response Exceeding Ferroelectrics Dimensionality Limit. *Adv. Funct. Mater.* **2026**, *36* (28), No. e23973.
(22) Kuwata, N.; Lu, X. L.; Miyazaki, T.; Iwai, Y.; Tanabe, T.; Kawamura, J. Lithium diffusion coefficient in amorphous lithium phosphate thin films measured by secondary ion mass spectroscopy with isotope exchange methods. *Solid State Ionics* **2016**, *294*, 59−66.
(23) Xie, J.; Imanishi, N.; Matsumura, T.; Hirano, A.; Takeda, Y.; Yamamoto, O. Orientation dependence of Li-ion diffusion kinetics in $LiCoO_2$ thin films prepared by RF magnetron sputtering. *Solid State Ionics* **2008**, *179* (9-10), 362−370.
(24) Kresse, G.; Furthmuller, J. Efficient iterative schemes for ab *initio* total-energy calculations using a plane-wave basis set. *Phys. Rev. B* **1996**, *54* (16), 11169−11186.
(25) Kresse, G.; Joubert, D. From ultrasoft pseudopotentials to the projector augmented-wave method. *Phys. Rev. B* **1999**, *59* (3), No. 1758.
(26) Steiner, S.; Khmelevskyi, S.; Marsmann, M.; Kresse, G. Calculation of the magnetic anisotropy with projected-augmented-wave methodology and the case study of disordered Fe1-xCox alloys. *Phys. Rev. B* **2016**, *93* (22), No. 224425.
(27) Perdew, J. P.; Burke, K.; Ernzerhof, M. Generalized gradient approximation made simple. *Phys. Rev. Lett.* **1996**, *77* (18), No. 3865.
(28) Monkhorst, H. J.; Pack, J. D. Special points for Brillouin-zone integrations. *Phys. Rev. B* **1976**, *13* (12), No. 5188.
(29) Liechtenstein, A. I.; Anisimov, V. I.; Zaanen, J. Density-functional theory and strong interactions: Orbital ordering in Mott-Hubbard insulators. *Phys. Rev. B* **1995**, *52* (8), No. R5467.
(30) Grimme, S. Semiempirical GGA-type density functional constructed with a long-range dispersion correction. *J. Comput. Chem.* **2006**, *27* (15), 1787−1799.
(31) Henkelman, G.; Arnaldsson, A.; Jónsson, H. A fast and robust algorithm for Bader decomposition of charge density. *Comput. Mater. Sci.* **2006**, *36* (3), 354−360.
(32) Makhoul-Mansour, M. M.; Maraj, J. J.; Sarles, S. A. Bioderived materials for stimuli-responsive, adaptive, and neuromorphic systems: A perspective. *J. Compos. Mater.* **2022**, 659−678.
(33) Moorsom, T.; Rogers, M.; Scivetti, I.; Bandaru, S.; Teobaldi, G.; Valvidares, M.; Flokstra, M.; Lee, S.; Stewart, R.; Prokscha, T.; et al. Reversible spin storage in metal oxide-fullerene heterojunctions. *Sci. Adv.* **2020**, *6* (12), No. eaax1085.
(34) Rogers, M.; Habib, A.; Teobaldi, G.; Moorsom, T.; Johansson, J. O.; Hedley, L.; Keatley, P. S.; Hicken, R. J.; Valvidares, M.; Gargiani, P.; et al. A Hybrid Magneto-Optic Capacitive Memory with Picosecond Writing Time. *Adv. Funct. Mater.* **2023**, *33* (13), No. 2212173.
(35) Andrew, P.; Barnes, W. L. Energy transfer across a metal film mediated by surface plasmon polaritons. *Science* **2004**, *306* (5698), 1002−1005.
(36) Mishra, K. C.; Collins, J. Dipole-Dipole Non-Radiative Energy Transfer Mediated by Surface Plasmons on a Metallic Interface. *ECS J. Solid State Sci. Technol.* **2019**, *8* (2), R27−R35.
(37) Bastos, J. P.; Voroshazi, E.; Fron, E.; Brammertz, G.; Vangerven, T.; Van der Auweraer, M.; Poortmans, J.; Cheyns, D. Oxygen-Induced Degradation in C_{60}-Based Organic Solar Cells: Relation Between Film Properties and Device Performance. *ACS Appl. Mater. Interfaces* **2016**, *8* (15), 9798−9805.
(38) Ito, A.; Morikawa, T.; Takahashi, T. Photo-induced polymerization and oxidation of C_{60} observed by photoelectron spectroscopy. *Chem. Phys. Lett.* **1993**, *211* (4−5), 333−336.
(39) Talyzin, A. V.; Dubrovinsky, L. S.; Le Bihan, T.; Jansson, U. *In situ* Raman study of C_{60} polymerization at high pressure high temperature conditions. *J. Chem. Phys.* **2002**, *116* (5), 2166−2174.
(40) Qin, Y. F.; Xu, J. L.; Liang, Z. W.; Teng, H. J.; Zhan, D.; Xu, H. Raman Spectroscopy of Fullerenes: From C60 to Functionalized Derivatives. *Molecules* **2025**, *30* (3), No. 738.
(41) Lee, C. H.; Yu, G.; Moses, D.; Srdanov, V. I. Dynamics of photoexcited carriers in pristine oxygen-free C60 films: Study of the time-resolved transient photoconductivity. *Synth. Met.* **1995**, *70* (1-3), 1413−1414.
(42) Hu, L.; Liu, F. H.; Quan, Q. L.; Lu, C. X.; Yu, S. J.; Li, L. W. Strained van der Waals Metallic Magnet for Photomagnetic Modulation and Spin Photodiode Application. *Adv. Funct. Mater.* **2024**, *34* (49), No. 2409085.
(43) Cadiz, F.; Lagarde, D.; Tao, B.; Frougier, J.; Xu, B.; Devaux, X.; Migot, S.; Wang, Z. G.; Han, X. F.; George, J. M.; et al. Electrical detection of light helicity using a quantum-dot-based hybrid device at zero magnetic field. *Phys. Rev. Mater.* **2020**, *4* (12), No. 124603.
(44) Safarov, V. I.; Rozhansky, I. V.; Zhou, Z. Q.; Xu, B.; Wei, Z. M.; Wang, Z. G.; Lu, Y.; Jaffres, H.; Drouhin, H. J. Recombination Time Mismatch and Spin Dependent Photocurrent at a Ferromagnetic-Metal-Semiconductor Tunnel Junction. *Phys. Rev. Lett.* **2022**, *128* (5), No. 057701.

https://doi.org/10.1021/acsami.6c02910
ACS Appl. Mater. Interfaces 2026, 18, 41881−41888